

Synergetic Lithium and Hydrogen Bonds Endow Liquid-Free Photonic Ionic Elastomer with Mechanical Robustness and Electrical/Optical Dual-Output

Lei Peng, Lei Hou,* and Peiyi Wu*

Photonic ionic elastomers (PIEs) capable of multiple signal outputs are intriguing in flexible interactive electronics. However, fabricating PIEs with simultaneous mechanical robustness, good ionic conductivity, and brilliant structure color still remains challenging. Here, the limitations are broken through introducing the synergistic effect of lithium and hydrogen bonds into an elastomer. In virtue of lithium bonding between lithium ions and carbonyl groups in the polymer matrix as well as hydrogen bonding between silanol on the surface of silica nanoparticles (SiNPs) and ether groups along polymer chains, the PIEs demonstrate mechanical strength up to 4.3 MPa and toughness up to 8.6 MJ m⁻³. Meanwhile, the synchronous electrical and optical output under mechanical strains can be achieved in the PIEs with the presence of dissociated ions contributed by lithium bond and non-close-packed SiNPs stabilized by the hydrogen bond. Moreover, due to their liquid-free nature, the PIEs exhibit extraordinary stability and durability, which can withstand extreme conditions including both high and low temperatures as well as high humidity. This work provides a promising molecular engineering route to construct high-performance photonic ionic conductors toward advanced ionotronic applications.

1. Introduction

Biological skins, wrapping the body of organisms and directly contacting the surrounding environments, can not only act as a protective layer with mechanical robustness but also help to perceive external stimuli and interact with the outside world through the transmitting of ion-based electrical signals.^[1] Inspired by the ion-conducting nature of biological skins, stretchable ionic conductors with skin-like capabilities, which show a series of sensations to pressure, strain, and temperature, have attracted extensive attention in human-machine interfaces,

soft robots, healthcare monitoring, etc.^[2] In addition to sensing via ion-based electrical signals, some biological skins could employ visual demonstration to interact with the external environment.^[3] Chameleons, for instance, present a remarkable capability to switch their skin color rapidly between camouflaged and bright states during social communications, including courtships and combats. It is generally believed that the color change of chameleon origins from actively tuning the lattice of guanine nanocrystals within a superficial thick layer of dermal iridophores, in which the fine structures constitute tunable photonic crystals.^[4] As a fascinating class of optical materials, photonic crystals are patterned with a periodicity in dielectric constant and could reflect a specific wavelength of the incident light, consequently displaying a structure color.^[5] When the periodic structure in photonic crystals varies under external stimuli, the structure colors can be simultaneously altered, which provides a useful method for the direct visualization of sensing stimuli.^[6] Compared with flexible electroluminescent devices which require high voltages,^[7] photonic ionic conductors provide a low-energy strategy for the design of multifunctional sensors. Thus, inspired from biological skins, the exploration of skin-like photonic ionic conductors with dual-signal output features is highly desired for flexible electronics.

Recent developments in artificial skins have revealed strategies to endow stretchable ion conductors with color change abilities, achieving both ionic and optical reporting signals under external perturbations.^[8] For example, hydrogel networks embedded with artificial reflective plates have been developed as chromotropic ionic skins, which could fulfill the electrical response and optical visualization synchronously to multiple stimuli, such as strain, tactile sensation, temperature, and IR light.^[9] More recently, photonic ionogels, constructed from the combination of ionic liquid (IL) and photonic elastomers, have been demonstrated with synergistically optical and electrical output under mechanical strain in harsh and complex environmental conditions.^[10] Despite the broad applicability of hydrogels or ionogels for flexible ionic conductors, due to the presence of solvents (water or IL), hydrogels suffer from inherent water evaporation in ambient conditions while ionogels face the problem of IL leakage under mechanical forces.^[11] Moreover,

L. Peng, L. Hou, P. Wu
 State Key Laboratory for Modification of Chemical Fibers and Polymer Materials
 College of Chemistry and Chemical Engineering
 Donghua University
 Shanghai 201620, P. R. China
 E-mail: houlei@dhu.edu.cn; wupeiyi@dhu.edu.cn

L. Hou
 National Innovation Center of Advanced Dyeing & Finishing Technology
 Tai'an, Shandong 271000, P. R. China

The ORCID identification number(s) for the author(s) of this article can be found under <https://doi.org/10.1002/adma.202211342>.

DOI: 10.1002/adma.202211342

the trade-off between the ionic conductivity and mechanical robustness with regard to solvent contents is also knotty, where increasing the content of solvents would usually result in the enhancement of ionic conductivity and weakening of mechanical strength.^[12] Under such circumstances, it is of great importance to develop liquid-free photonic ion skins with satisfactory ionic conductivity and mechanical properties.

In this work, we report the design and fabrication of robust, ion-conductive, and liquid-free photonic skins with synchronously ionic and optical output under mechanical strains by introducing a lithium salt into the photonic elastomer network, as inspired by polymer electrolytes for solid-state lithium-ion batteries. Herein, the elastic polymer matrix is based on poly(2-methoxyethylacrylate) (PMEA), which demonstrates a biocompatible hydrophobic polymer with low glass transition temperature and possesses both ester and ether groups in the repeat unit, providing abundant interaction sites along the polymer chains for constructing composite elastomers. Through delicately manipulating the molecular interactions within the elastic PMEA network, nanoparticles, and charge carriers, the conflict among the mechanical properties, ionic conductivity, and structure color can be well balanced. Specifically, the lithium bond between lithium ions and carbonyl groups in PMEA, on the one hand, acts as additional cross-linkers, which increases the mechanical strength, and on the other hand, helps the disassociation of lithium salt and facilitates the interchain Li⁺ transfer^[13] under an external electric field, which improves the ionic conductivity. In addition, hydrogen bonds between hydroxyl groups on the surface of silica nanoparticles (SiNPs) and ether groups along the PMEA chains contribute to stabilizing of non-close-packed SiNPs separated by the elastomeric matrix,^[14] which results in brilliant structure color, and toughening of the photonic elastomer under deformation, where increasing the content of SiNPs would simultaneously improve the stress and the strain at break. Consequently, the resultant photonic ionic elastomers (PIEs) demonstrate excellent mechanical robustness with breaking strength up to 4.3 MPa and toughness up to 8.6 MJ m⁻³, much more superior to previously reported photonic materials with flexibility and ionic/electrical conductivity. Once under a mechanical strain, the lattice spacing and resistance of the PIEs could be altered, leading to a synchronous optical and ionic response. Due to their liquid-free nature, the PIEs are free from solvent evaporation, freezing, or leakage^[11,15] and exhibit extraordinary stability and durability, which could withstand extreme conditions including a wide temperature range (-35–180 °C) as well as high humidity (90% RH). The PIEs developed herein provide a facile method to fabricate mechanically robust and ion-conductive photonic elastomers with multi-signal outputs and demonstrate great potential in soft robots, wearable electronics, human-machine interfaces, etc.

2. Results and Discussion

2.1. Preparation and Characterization of PIEs

Figure 1a displays the two-step preparation of PIEs. First, a photonic elastomer is synthesized through in situ poly-

merization of 2-methoxyethylacrylate (MEA) in the presence of SiNPs, defined as PE_{x-y} (x is the molar ratio percentage of cross-linker to monomer, and y is the mass fraction of SiNPs in the elastomer). Herein, the rigid SiNPs were embedded in the PMEA elastomer to form non-close-packed crystals so as to mimic the iridophore structure with varied structure colors.^[14,16] In the precursor solution of MEA/SiNPs, ether groups of MEA could interact with hydroxyl groups on the surface of SiNPs through hydrogen bonding, forming a dense solvation layer around SiNPs and contributing to the stable array of SiNPs.^[17] After polymerization, the array is fixed in the PMEA elastomer and consequently, a composite photonic elastomer exhibiting reflective color is achieved (Figure S1, Supporting Information). Time-dependent FTIR spectra have been collected to monitor the photopolymerization process (Figure S2, Supporting Information), where the intensity of the bands (1637 and 1620 cm⁻¹) related to the carbon-carbon double bond of monomer MEA decreases intensely with time, representing the polymerization of MEA into PMEA. After polymerization for 15 min, the bands related to C=C bond disappear, indicating complete polymerization. Second, a lithium salt, bis(trifluoromethane)sulfonimide (LiTFSI), is introduced into the photonic elastomer through a facile solvent-assisted infusion strategy in order to endow the elastomer with ionic conductivity as well as fine-tuned mechanical performance. Herein, the solvent-assisted infusion strategy is used instead of polymerizing MEA in the presence of both SiNPs and LiTFSI, due to the fact that directly adding LiTFSI in the precursor solution before polymerization would lead to the sedimentation of SiNPs, as shown in Figure S3 (Supporting Information). It is supposed that LiTFSI could interact strongly with MEA and interrupt the interactions between MEA and SiNPs, thus resulting in the destabilization and aggregation of SiNPs. A series of PIE_m (m represents the mass fraction of LiTFSI in the elastomer) with varied LiTFSI content can be achieved by immersing the photonic elastomer in LiTFSI/ethanol solutions with different concentrations to an equilibrium. On the one hand, LiTFSI could partially dissociate into Li⁺ and TFSI⁻ with the help of ion-dipolar interactions (so-called “lithium bond”) between PMEA and Li⁺, facilitating the Li⁺ transportation among polymer chains and providing the PIEs with good ionic conductivity. On the other hand, Li⁺ could act as a physical cross-linker between PMEA chains through lithium bonds to improve the mechanical performance of the elastomer.^[18] Meanwhile, the structure color remains after the incorporation of LiTFSI (Figure S1, Supporting Information).

Figure 1b displays the scanning electron microscope (SEM) images of the surface (i) and cross-section (ii) of PIE₉, where the molar ratio of cross-linking agent to monomer is 0.5%, SiNPs content is 50 wt.% and the particle size of SiNPs is 167 nm. The SEM images of PIE₉ are similar to that of the PEs without LiTFSI (Figure S4, Supporting Information), demonstrating the non-close-packed array of SiNPs embedded in the PMEA matrix. In addition, there is no obvious aggregation of the lithium salt in the elastomer, indicating good compatibility between LiTFSI and PMEA. Furthermore, PIE₉ with various brilliant structure colors could be obtained by regulating the particle size of SiNPs. With increasing the diameter of SiNPs from 128 to 167 nm (Figure S5, Supporting Information), the structural color of PIE₉ changes from blue to green and red,

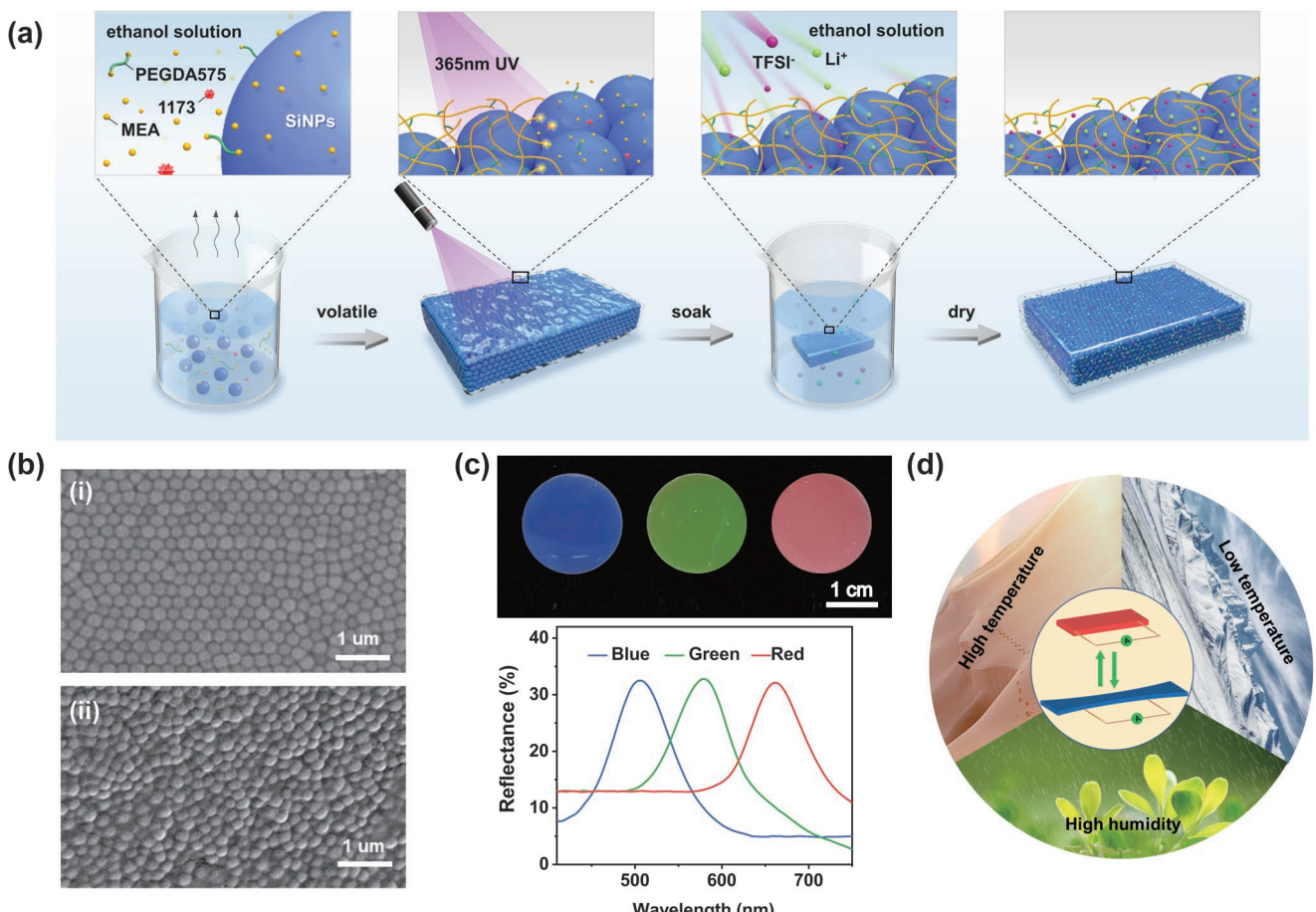


Figure 1. a) Schematic illustration of the preparation of PIEs. b) SEM images of the red PIE₉: surface (i) and cross-sectional (ii) view. c) Photographs and d) reflection spectra of PIE₉ with different structural colors. e) Demonstration of PIEs as strain sensors under harsh environmental conditions.

as demonstrated in Figure 1c. In the corresponding reflectance spectra (Figure 1d), the reflection wavelength peaks of PIE₉ increase from 505 to 660 nm, which is well consistent with the appearance in the photograph and confirms the convenient tune of structure color by changing particle size. By combining structure color and ionic conductivity in the elastomer, the PIEs could be used as flexible strain sensors displaying simultaneous optical and electrical output, holding great potential in the field of ionic skins. Moreover, the PIEs prepared herein can work in various harsh environments, including high temperature, low temperature as well as high humidity due to the lack of liquid solvents (liquid-free), which greatly broadens the applied scenario of multifunctional stretchable electronics. (Figure 1e).

In order to optimize the mechanical performance of PIEs, which is crucial for the practical use of PIEs as ionic skins. The effect of chemical cross-linker length, cross-linking density, SiNPs, and LiTFSI content on the mechanical properties of the elastomer has been examined. Figure S6 (Supporting Information) indicates that longer cross-linker length leads to more ductile elastomer. Considering the overall performance of the elastomer, including Young's modulus (E), breaking strain(ϵ_b), and breaking strength (σ_b) (Figure S7, Supporting Information), we choose PEGDA of molecular weight 575 for further study. For the PEs without LiTFSI, increasing the molar ratio

of PEGDA575 to MEA will lead to higher cross-linking density, making the PEs more brittle with higher E and σ_b but obviously lower ϵ_b (Figure 2a; Figure S8, Supporting Information). Meanwhile, a notable toughening of the composite elastomer is observed with increasing the content of SiNPs. As shown in Figure 2b, both σ_b and ϵ_b are significantly improved with increasing the amount of SiNPs (Figure S9, Supporting Information), which, in some extent, overcomes the conflict between the strength and toughness of an elastomer. Such a behavior could be probably rooted from: i) interfacial interactions between the PMEA chains and SiNPs and ii) collision and friction of SiNPs under large strains.^[17,19] It is noted that there exists a shoulder at $\approx 200\%$ strain followed by a plateau region where the stress almost maintains with strain increasing in the tensile stress-strain curves of PE_{0.5–40} and PE_{0.5–50}. We tentatively propose that such a shoulder could be related to the re-arrangement of SiNPs under relatively large deformation^[19a] and the plateau might be originated from the subsequent entropic extension of polymer chains adsorbed on the surface of SiNPs.^[20] Once the entropic extension is complete, the system stiffens as stress is transferred to relatively rigid chemical cross-linkings. In addition, a decrease in stress is observed after the shoulder and the situation is more obvious for PE_{2–50} of higher cross-linking density. Resembling the polydomain-to-monodomain

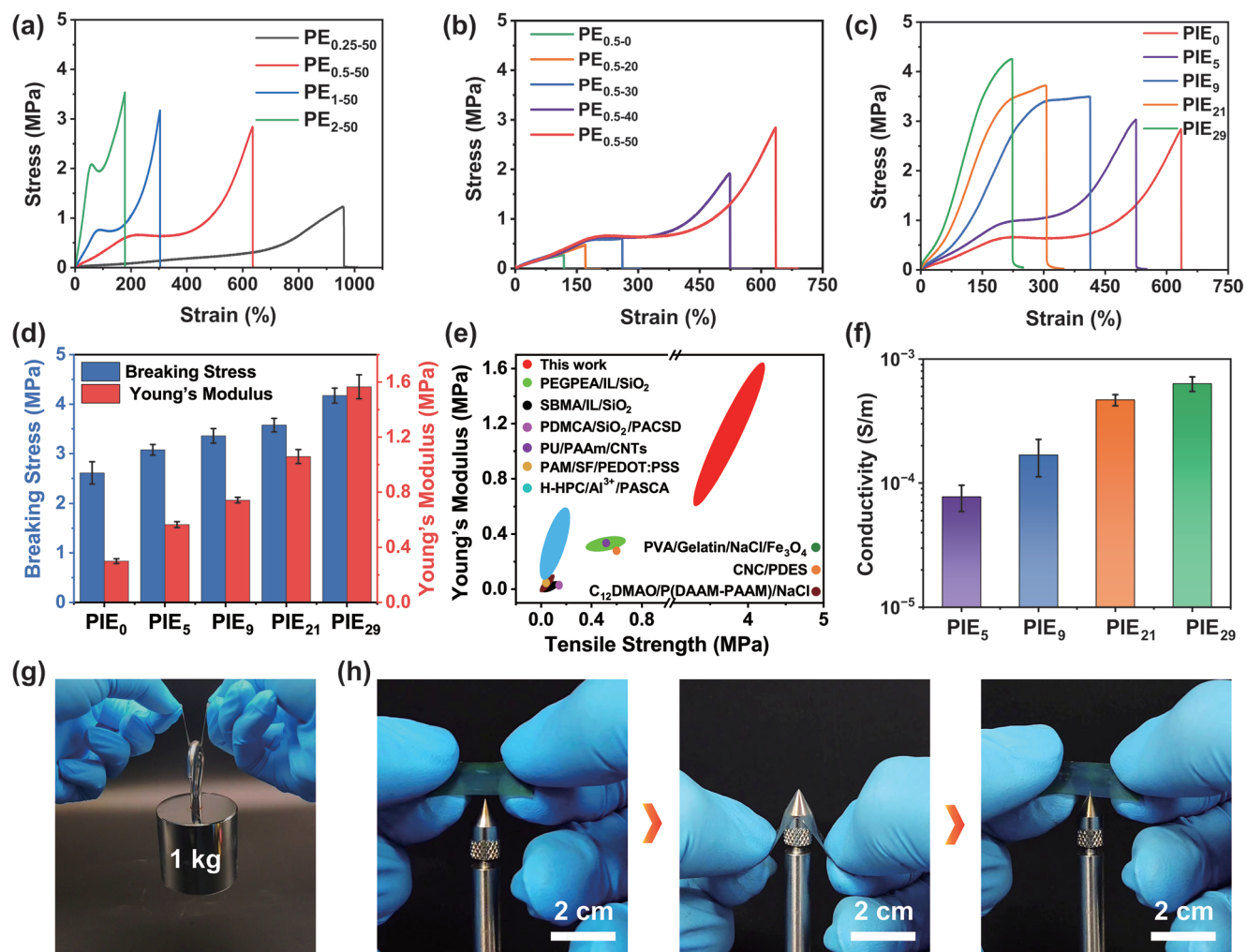


Figure 2. Tensile stress-strain curves of PEs with different content of a) cross-linker and b) SiNPs. c) Tensile stress-strain curves and d) the corresponding breaking stress and Young's modulus of the PIEs with different content of LiTFSI. e) Tensile strengths and Young's modulus of PIEs compared with the reported ion/electron conductive photonic gels. f) Ionic conductivity of the PIEs with various LiTFSI contents. g) Picture of 0.1 g PIE₉ loading weight of 1 kg. h) Pictures showing that the PIE₉ could tolerate puncture under large deformation. The diameter of SiNPs is 150 nm.

transition of liquid crystalline elastomers,^[21] we could attribute such a decrease in stress to the structural adjustment of SiNPs, such as rotation, under stretching. Figure S10 (Supporting Information) infers that the tensile stress-strain curves could gradually recover after a certain waiting time, indicating the rearrangement and structural adjustment of SiNPs under large strains is reversible. Herein, the PE_{0.5 – 50} presents excellent mechanical performance with σ_b of 2.8 MPa and ϵ_b of 635% as well as brilliant structure color, which will be selected for further compounding with LiTFSI to prepare PIEs.

Figure 2c shows the stress-strain curves of PIEs with different LiTFSI loading, demonstrating that PIEs are stretchable and hold elastic behavior. Moreover, LiTFSI presents a strengthening effect on the mechanical performance of the elastomer and more LiTFSI results in stiffer PIEs. More specifically, E and σ_b of the photonic elastomer increase from 0.3 and 2.8 MPa to 1.6 and 4.3 MPa, respectively, after loading of 29 wt.% LiTFSI (Figure 2d), and the toughness is up to 8.6 MJ m⁻³ (Figure S11, Supporting Information). In the meantime, the presence of

LiTFSI endows the elastomer with ionic conductive nature, and higher LiTFSI content leads to increased ionic conductivity, as displayed in Figure 2f and Figure S12 (Supporting Information). It could be explained by the fact that ionic conductivity is typically proportional to the effective number of mobile ions.^[18] The conductivities of PIEs are also examined on a multimeter (Figure S13, Supporting Information), which are comparable to that extracted from impedance measurements, confirming that the main contribution to electrical properties, such as resistance, is the movement of ions in PIEs. Herein, it should be noted that the incorporation of LiTFSI could simultaneously improve the mechanical performance and ionic conductivity of PIEs, which is in full contrast with the situation of solvent-based ionic conductors, such as hydrogels and ionogels. Generally, hydrogels or ionogels face a trade-off between mechanical strength (E and σ_b) and ionic conductivity, where higher content of solvent (water or ionic liquid) results in improved ionic conductivity while degradation in mechanical strength. From this point of view, the liquid-free PIEs present a promising

strategy for fabricating mechanical robust elastomers with good ionic conductivity. Comparing with reported ion/electron conductive photonic gels, the PIEs herein demonstrate obviously better mechanical robustness (Figure 2e).^[9,10,22] In addition, the mechanical performance of PIEs could be conveniently regulated with LiTFSI content, SiNPs content as well as cross-linking density. As shown in Figure 2g and Movie S1 (Supporting Information), 0.1 g PIE₉ with a width of 0.5 cm and thickness of 300 μ m could easily lift a weight of 1 kg, which is 10 000 times its own weight. Furthermore, the tough PIE₉ can withstand puncture under large deformation (Figure 2h, Movie S2, Supporting Information), benefiting the practical use as ionic skins.^[23] As shown in Figure S14 (Supporting Information), the PIE₉ could tolerate higher puncture force as compared with PMEA elastomer, PIE₀ as well as VHB tape, probably due to the increased toughness with the presence of synergistic lithium bonds and hydrogen bonds in the elastomer.

2.2. Molecular Interactions in the PIEs

Infrared spectroscopy is employed to validate the internal interactions responsible for the mechanical properties of the PIE₉. Herein, we will mainly focus on the bands in the regions of 1770–1680 and 990–900 cm^{-1} , which are related to the stretching vibration of C=O of PMEA and Si—OH of SiNPs, respectively. Second derivative curves of the corresponding FTIR spectra, where the sharpened minima are related to the maxima in the original absorption spectra, are plotted to enhance the spectral resolution. As shown in Figure 3a, the $\nu(\text{C=O})$ band exhibits nearly no change with the presence of SiNPs. While, after

the incorporation of LiTFSI into the photonic elastomer, an apparent shoulder peak appears at $\approx 1710 \text{ cm}^{-1}$, indicating the formation of a different non-covalent bond with regard to C=O groups. Considering the potential interactions within LiTFSI and C=O, it is proposed that a lithium bond forms between Li⁺ and C=O groups.^[24] For the lithium bond, it usually occurs between lithium ions and polar groups and can be categorized into ion-dipole interactions.^[25] Quite different from an ionic bond, the lithium bond shows much smaller bonding energy and negligible negative charge transfer.^[26] Owing to the large radius and metallic nature of Li, the lithium bond possesses no saturation or directionality limitations.^[26] In the PIE₉, the coordination number of carbonyl groups with Li⁺, which can be obtained by evaluating the area ratio of lithium bonded carbonyl band to the total area of the carbonyl band (Figure S15, Supporting Information) according to previous pieces of literature,^[27] is calculated to be ≈ 2 . Under such a circumstance, Li⁺ could act as a physical cross-linker of PMEA chains through lithium bonding, which contributes to the enhanced mechanical performance of the PIEs. For the $\nu(\text{Si—OH})$ region, the peaks exhibit a frequency shift and new bands at lower wavenumbers can be observed in both PE_{0.5 – 50} and PIE₉ systems, suggesting the hydrogen bonding between Si—OH groups on the surface of SiNPs and polar groups along PMEA chains. Since the incorporation of SiNPs in the PMEA matrix brings neglect changes in the shape of $\nu(\text{C=O})$, it is inferred that Si—OH groups mainly interact with ether groups of PMEA through hydrogen bonding.

Temperature-dependent FTIR spectroscopy, which allows for the investigation of subtle changes in specific groups from the molecular level, is employed to study the variations of $\nu(\text{C=O})$

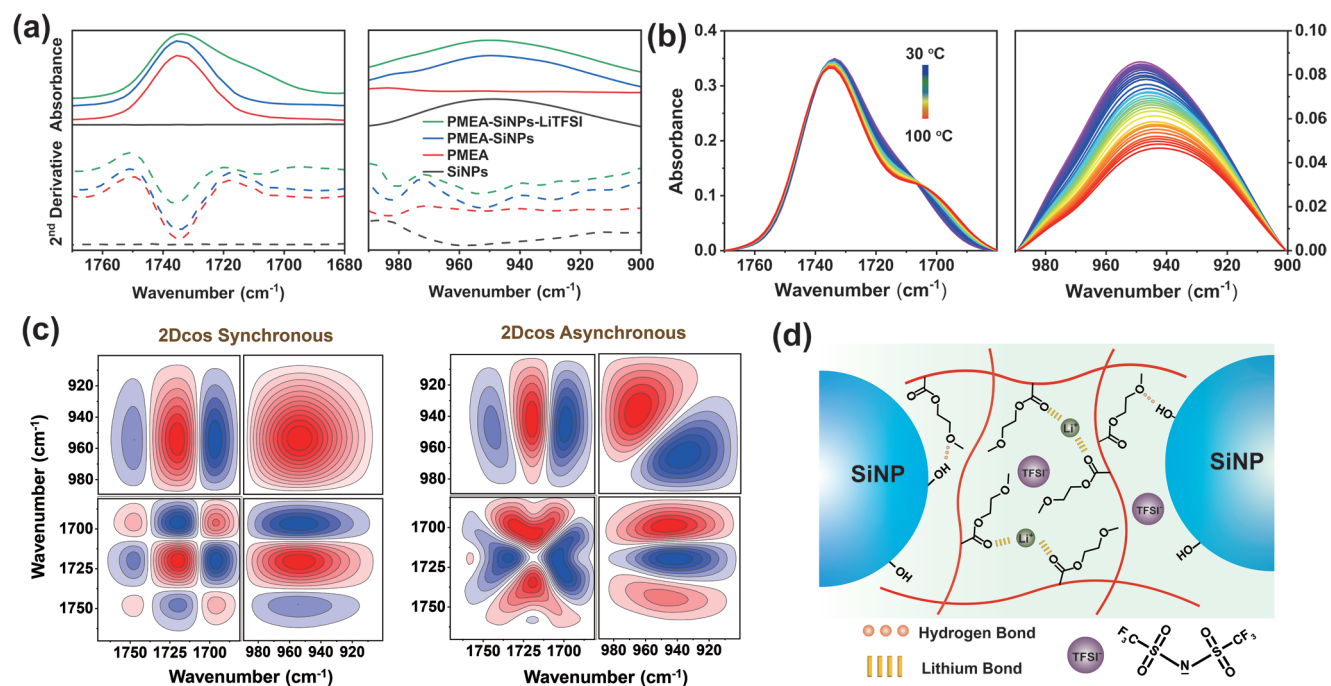


Figure 3. a) FTIR spectra and corresponding second derivative curves of SiNPs (black), PMEA (red), PMEA-SiNPs (PE_{0.5 – 50}) (blue), and PMEA-SiNPs-LiTFSI (PIE₉) (green). b) The temperature-dependent FTIR spectra of the PIE₉ during heating from 30 to 100 °C in the regions of $\nu(\text{C=O})$ and $\nu(\text{Si—OH})$. c) 2Dcos synchronous and asynchronous spectra generated from (b). In 2Dcos spectra, the warm colors (red) represent positive intensities, while cold colors (blue) represent negative ones. d) Schematic diagram of internal interactions of PIEs.

and $\nu(\text{Si}-\text{OH})$ bands upon heating. As displayed in Figure 3b and Figure S16 (Supporting Information), the bands in the two regions exhibit frequency shifts with temperature increasing, implying the changes of molecular interactions with regard to C=O and Si—OH groups. Particularly, it is noticed that the peak related to C=O groups involved in lithium bonds presents a red shift upon heating, hinting strengthening of the lithium bond. Taking the hygroscopicity of LiTFSI into consideration, a small amount of water molecules remains in the PIE₉ at room temperature, which might to some extent interfere the forming of lithium bond between Li⁺ and C=O. During the heating process, water molecules would evaporate, as confirmed by the intensity decreasing of $\delta(\text{O}-\text{H})$ band of water at $\approx 1640 \text{ cm}^{-1}$ (Figure S17, Supporting Information), thus resulting in the strengthening of the lithium bond. 2D correlation spectroscopy (2Dcos),^[28] whose principles are described in the Supporting Information, is generated from the temperature-variable FTIR spectra to recognize fine structures in the PIE₉. In the 2D asynchronous spectra, splitting bands of 1733, 1720, and 1700 cm^{-1} corresponding to C=O groups along PMEA chains and subtle bands at 966 and 937 cm^{-1} related to Si—OH groups on the surface of SiNPs have been identified, providing details on the internal interactions in the PIE₉. Herein, the recognized bands at 1733, 1720, 1700, 966 and 937 cm^{-1} could be tentatively assigned to dipole-dipole interacted C=O, weakly lithium bonded C=O, strongly lithium bonded C=O, weakly hydrogen-bonded Si-OH and strongly hydrogen bonded Si—OH, respectively, further confirming the dominant role of lithium and hydrogen bonds in the PIE₉. For clarity, a schematic illustration of various molecular interactions in the PIEs is demonstrated in Figure 3d.

To further examine the internal interactions of PIEs, solid-state NMR and X-ray photoelectron spectra (XPS) measurements have been carried out. In the ⁷Li NMR spectra (Figure S18a, Supporting Information), the peak of LiTFSI has a shift ≈ 0.6 ppm with the presence of PMEA and SiNPs, revealing the strong binding between Li⁺ and PMEA.^[26,29] In addition, the appearance of the band of Li—O in XPS of PMEA-LiTFSI and PMEA-SiNPs-LiTFSI (Figure S18b, Supporting Information) further confirms the lithium bond formation between Li⁺ and C=O in PMEA. For the hydrogen bonding between Si-OH and PMEA, obvious chemical shifts can be observed for the silanols-related proton resonance peaks (Figure S19a, Supporting Information) after compositing with PMEA or PMEA-LiTFSI. Moreover, the binding energy of Si exhibits an obvious shift in XPS of SiNPs as compared with that in PMEA-SiNPs and PMEA-SiNPs-LiTFSI elastomers (Figure S19b, Supporting Information), further substantiating the interaction between SiNPs and PMEA.

2.3. Synergistically Optical and Electrical Outputs as Ionic Skins

Profiting from the structure color and ionic conductivity, the designed PIEs' own dual-signal responses of color and resistance change under stretching, where the color variation comes from the non-close-packed SiNPs and resistance variation originates from the conductive nature. To validate the dynamic color-switching behavior, the PIE₉ with red structure

color under different tensile strains has been investigated. As displayed in Figure 4a and Movie S3 (Supporting Information), the structure color exhibits a gradual shift from red to green, and finally to blue with the increase of tensile strain, demonstrating the excellent mechanochromic property. In addition, the performance remains the same after multiple stretch recovery cycles, demonstrating the robustness of the PIE₉ (Movie S4, Supporting Information). It is noted that the brilliant structure color disappears at large deformations, which could be explained by that the color has been blueshifted out of the visible light region. Figure 4b records the corresponding reflection spectra during the stretching process, where the reflection wavelength presents a continuous blueshift from 610 to 480 nm when the strain increases from 0 to 80%, confirming the color-changing behavior. Herein, the color change can be explained by Bragg's diffraction Equation (1):^[30]

$$\lambda = 2nd \sin \theta \quad (1)$$

where λ is the reflection wavelength, n is the effective refractive index, d is the lattice spacing, and θ is the incidence angle. During stretching, the cross-section of the elastomer shrinks, resulting in the decrease of the lattice spacing of nanoparticles in the vertical direction and leading to the blueshift of the maximum reflection wavelength, as illustrated schematically in Figure 4c. The change in the lattice spacing of SiNPs vertical to the stretching direction in the elastomer is further confirmed from SEM images (Figure 4c; Figure S20, Supporting Information). After relaxation, the recovery of the lattice spacing (Figures S20,S21, Supporting Information) results in the structural color switching back to the original state due to the elasticity of the PIE₉ (Figure S22, Supporting Information). During repeated loading/unloading cycles between $\varepsilon = 0\%$ and 50%, the reflection wavelength of the PIE₉ exhibits a stable switching between 610 and 520 nm (Figure 4d), demonstrating excellent durability and reversibility. Benefiting from the ionic conductivity and elasticity, PIE₉ can be utilized as a reliable strain sensor through output resistance changes. As observed in Figure S23 (Supporting Information), the PIE₉ presents a rapid increase of resistance during stretching to 400% with gauge factors (GF) in the small and large strain ranges of 1.1 and 2.3, respectively. Cyclic stretching of the PIE₉ to fixed strains of 20, 40, 60, 80, and 100% resulted in stable, repeatable yet strain-dependent resistance changes (Figure 4e), demonstrating the capability of PIEs in discerning deformation degrees. Furthermore, the PIE₉ displays excellent stability and repeatability in the resistance change during continuous stretching for 1000 cycles under the fixed strain of 80% (Figure 4f), showing its remarkable durability. Herein, the reversibility of the continuous color and resistance changes are examined after the first stretching/releasing cycle. Then, a dual-signal output of the PIE₉ upon stretching is achieved by combining the color-switching and resistance variation. As shown in Figure 4g, the reflection wavelength and relative resistance exhibit a linear response to tensile strain with excellent reversibility, where the mechanochromic sensitivity is $\approx 1.6 \text{ nm } \%^{-1}$ and the GF is ≈ 1.1 . In a dynamic responsive process, the resistance and reflection wavelength of the PIE₉ display near-perfect synchronization and reversibility over the 0–80% strain range due to the excellent mechanical robustness and structure stability (Figure 4h).

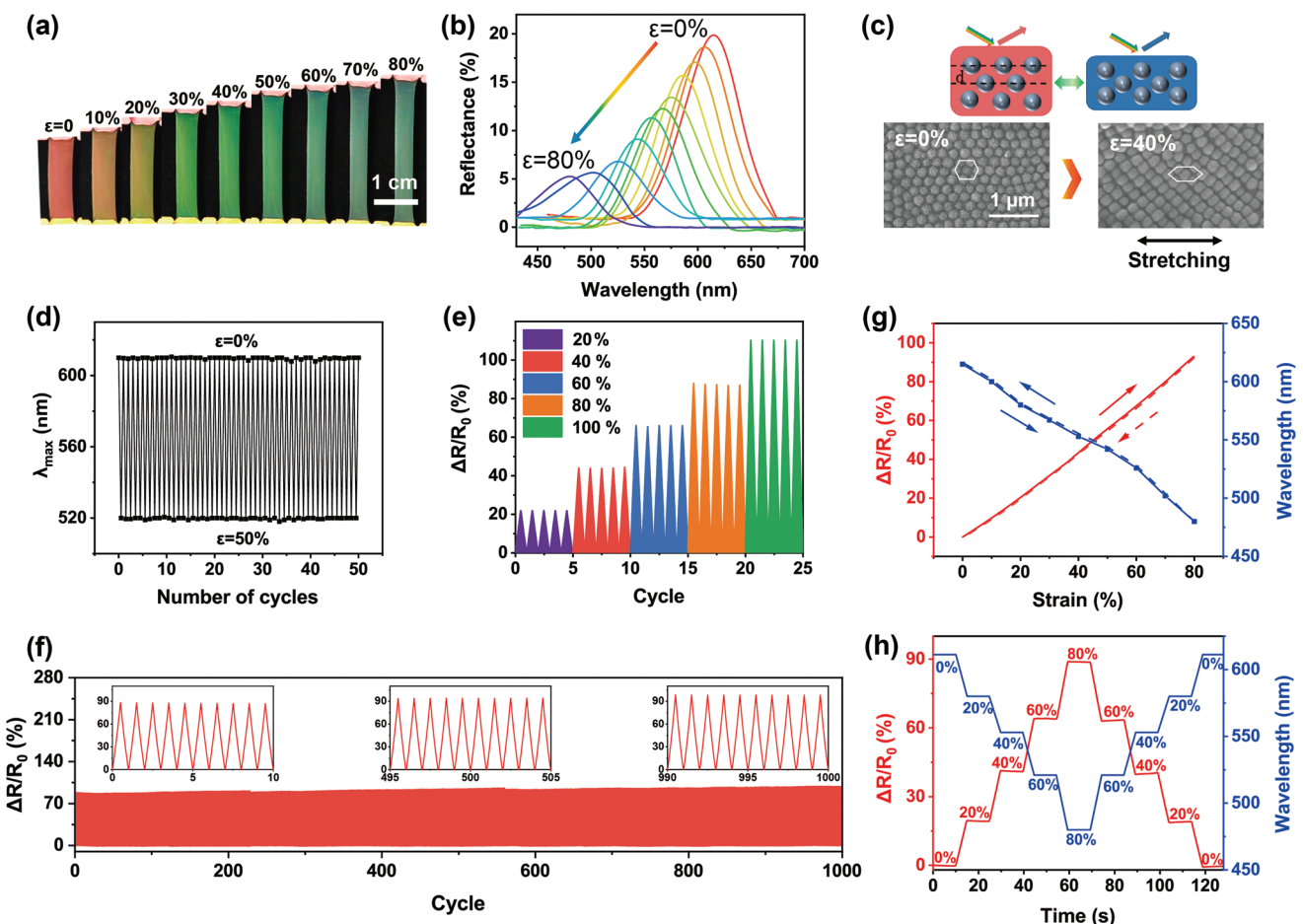


Figure 4. a) Photographs and b) reflection spectra of the PIE₉ under different tensile strains. c) SEM images and schematic illustration showing the mechanochromic mechanism of PIEs. d) Reversible change of λ_{max} of PIE₉ during stretching/releasing cycles at a strain of 50%. e) Realtime response curves measured at fixed strains of 20, 40, 60, 80, and 100% for five cycles each. f) Relative resistance variations of the PIE₉ strain sensor upon stretching to 80% strain for 1000 cycles. λ_{max} and the relative resistance as a function of strain (g) and time (h) under cyclic stretching/releasing.

further confirming the application potential as an advanced wearable interactive device. The PIE₉ with simultaneous optical and ionic signal output under external strain holds great potential in high-performance ionic skins. For clarity, the comparison of PIEs with other strain sensor materials is demonstrated in Table S1 (Supporting Information).

As a proof-of-concept experiment, the PIE₉ is fixed on a finger to monitor the motions of human joints outputting synchronous visual and electrical signals (Figure 5a). In the case of finger bending, which leads to the PIE₉ stretching, the resistance, and structural color change immediately and simultaneously (Figure 5b). In addition, signals remain unchanged when the bending gesture maintains and return back to the initial state with the bending angle decreasing, indicating the reliability of utilizing the PIE₉ in recognizing joint motion. More specifically, for the finger joint bending in a small amplitude, the relative resistance increases by a stable value $\approx 12\%$ while the reflection wavelength shifts from 610 to 575 nm (Figure 5c,d), which can be observed by the naked eye that the structural color changes significantly from red to green. Furthermore, with a large amplitude of bending, the relative resistance increased by 30% and the reflection wavelength shifted

from 610 to 520 nm, leading to a switch of the structural color from red to blue (Figure 5e,f).

Due to the absence of solvent, the PIEs hold great advantages in using as an interactive sensor under critical circumstances. As confirmed by Thermogravimetry analysis (TGA) (Figure S24, Supporting Information), the liquid-free PIEs present high thermal stability with a negligible weight loss of $\approx 3\%$ before reaching 180 °C, which is far better than hydrogel-based conductors. In addition, due to the flexible chains of PMEA, the PIEs exhibit the glass transition temperature (T_g) in the range between -35 and -19 °C depending on the LiTFSI content (Figure S25, Supporting Information), probably owing to the higher content of LiTFSI leads to higher cross-linking density through lithium bond. On the basis of TGA and DSC results, the PIEs demonstrate a wide operating temperature window, from -35 to 180 °C. Figure S26 (Supporting Information) indicates that the PIE₉ is flexible under -25 °C. As substantiated in Figure 5g,h and Figure S27 (Supporting Information), the PIE₉ exhibits remarkably stable resistance changes accompanied by color switching stored between -27 and 180 °C. Even under 90% relative humidity (RH), the PIE₉ can still respond sensitively to the mechanical stretch with electrical and optical

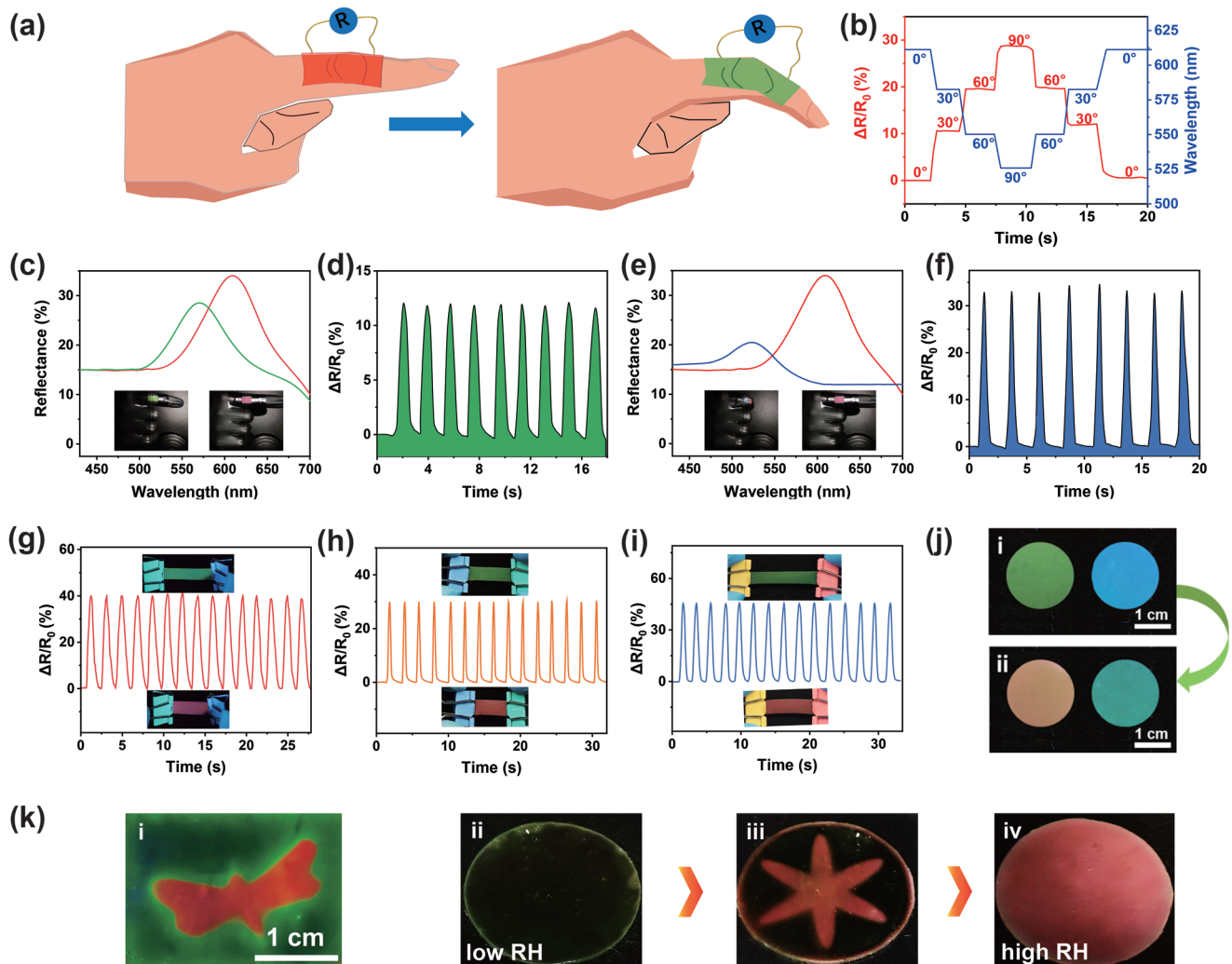


Figure 5. a) Schematic illustration showing the application of PIEs as an interactive sensor for tracking finger motion. b) Reversible changes in relative resistance and reflection wavelength with an angle of bending. Real photographs and corresponding reflectance spectra c,e) when monitoring joint movements of finger and corresponding signals of relative resistance change d,f). Real photographs and the response of the resistance signal of the sensor to detect the strain under g) high temperature (100 °C), h) low temperature (-18 °C), and i) at 90% RH. j) Real photos of PIE₉ with different SiNPs size at 20% (i) and 80% (ii). k) Real photos of PIEs with patterned structure color in response to RH. Patterns in (i) and (iii) are obtained through selective contact with high RH air using a mask.

outputs (Figure 5i). The long-time stability of PIE₉ can be also deduced by monitoring the weight change under various harsh conditions (Figure S28, Supporting Information). It should be noted that the PIE₉ could absorb moisture from ambient air due to the hygroscopicity of LiTFSI, as confirmed by the intensity increasing of $\delta(\text{O}-\text{H})$ band of water at $\approx 1640 \text{ cm}^{-1}$ when the RH increased from 20 to 80% (Figure S29, Supporting Information), making the PIE₉ humidity responsive. Meanwhile, the PIE₉ remains elastic with $G' > G''$ under high RH (Figure S30, Supporting Information). As shown in Figure 5j, the PIE₉ possesses varied structural colors under different RH. Specifically, the structure color of PIE₉ changes from blue to cyan and green to orange, respectively, with increasing the RH from 20 to 80%, which could be caused by the increased refractive index under higher RH (Figure S31, Supporting Information). The patterns of PIEs in response to RH are demonstrated in Figure 5k. More-

over, the ionic conductivity also increases with RH (Figure S32, Supporting Information). From the above points of view, the liquid-free PIEs provide a highly stable and durable platform with dual signal output under different external stimuli that could be used as wearable interactive sensors.

3. Conclusion

In this work, we report a facile method to fabricate liquid-free mechanically robust, and ion-conductive photonic elastomers with dual-signal outputs under external stimuli, demonstrating great potential as interactive sensors in the arena of flexible electronics. The multifunctional PIEs were achieved through delicately manipulating the hydrogen and lithium bond within the elastomer, which is confirmed through multi-dimensional

infrared-spectral analysis. To be more specific, the hydrogen bond between Si—OH groups on the surface of SiNPs and ether groups along PMEA chains contribute to the tough photonic elastomer with brilliant structure color while the lithium bond between Li⁺ and C=O of PMEA contribute to further improved mechanical feature with acquired ionic conductivity. Particularly, the engineered molecular interactions, to some extent, defeat the conflict among mechanical strength, ionic conductivity, and structure color for solvent-based ionic conductors. Holding excellent mechanical robustness, satisfied ionic conductivity, and brilliant structure color, the PIEs exhibit synchronous optical and ionic response with perfect reversibility under a mechanical strain, which leads to altered lattice spacing and resistance in the elastomer. Due to the solvent-free characteristic, PIEs could withstand extreme conditions including high temperatures, low temperatures as well as high humidity, showing extraordinary stability and durability. It is anticipated that the liquid-free PIEs would provide an effective strategy for the fabrication of high-performance ionic skins in the applications of human-machine interfaces, soft robots, smart textiles, and so on.

4. Experimental Section

Materials: 2-methoxyethylacrylate (MEA) was purchased from TCI chemical and purified by passing through an alumina column. Tetraethyl orthosilicate (TEOS) was purchased from TCI chemical. Poly(ethylene glycol) diacrylate (PEGDA) and bis(trifluoromethylsulfonyl) imide (LiTFSI) were purchased from Sigma-Aldrich. 2-hydroxy-2-methylpropiophenone (Irgacure 1173) was obtained from Aladdin Reagents. Carbon Black, ethanol (≥ 99.7 wt.%), and ammonia ($\text{NH}_3 \cdot \text{H}_2\text{O}$) were purchased from Sinopharm Chemical. All the reagents were used without further purification.

Preparation of Photonic Elastomers (PEs): The monodisperse SiNPs were prepared in the laboratory by a modified Stöber method.^[31] In a typical experiment for the synthesis of PEs, 0.5 g SiNPs containing 0.025 wt.% of carbon black were first dispersed in 5 g ethanol under Probe ultrasound (JY92-IIDN). Then, solutions containing 0.5 g MEA (monomer), 0.5 mg Irgacure 1173 (photoinitiator), and various amounts of PEGDA575 (chemical cross-linker) were mixed with the above dispersion and placed in a 70 °C oven for 12 h to evaporate ethanol.^[32] Finally, the precursor was infiltrated into a mold composed of two glass slides with 150-μm-thick spacers of polyimide tape (Kapton) and cured under UV light (365 nm) for 15 min.

Preparation of Photonic Ionic Elastomers (PIEs): PEs with varied LiTFSI content were prepared by immersing the PEs into solutions of LiTFSI in ethanol with different concentrations to an equilibrium state. The ethanol was removed by evaporating in a vacuum at 90 °C for 2 h. Finally, PIEs with structure color consisting of different LiTFSI contents were obtained.

Characterizations: The tensile tests of the sample were performed on a universal testing machine (UTM2103, Shenzhen Suns Technology) with a tensile rate of 5 min⁻¹. The samples of elastomers were cut into a rectangular shape of 15 mm in length and 5 mm in width. The thickness of the sample is 0.15 mm. Tensile tests were performed with a gauge length of 10 mm. Tensile tests of PIE₉ under -25 °C were performed with DMA (TA Q800). Cross-section and surface images of PEs and PIEs were taken on an SEM (Hitachi, Japan SU8230). DLS tests were carried out by particle size analyzer (Nano-ZS). TGA tests were performed on TA TGA550 with a temperature scanning range from 30 to 600 °C under Nitrogen flow (heating rate = 10 °C min⁻¹). Differential scanning calorimetry (DSC) tests during the heating process were collected using TA DSC250 in the temperature scanning range between -60 and 80 °C with a scanning rate of 10 °C min⁻¹.

(nitrogen flow). The ionic conductivity was characterized by EIS under the frequency range from 10⁶ to 0.1 Hz (PIEs were sandwiched between two stainless sheets of steel), and calculated through the following formula:^[33]

$$\sigma = \frac{1}{S \times R_b} \quad (2)$$

where I is the thickness of the sample; R_b is the bulk resistance, and S is the area of the PEs. Resistance changes of PEs-based ionic skin were monitored on a multimeter (Tektronix, DMM 4050). Reflectance spectra were obtained by a USB2000 fiber optical spectrometer (Ocean Optics). The relative humidity was controlled by the temperature and humidity chamber (MHW-200). FTIR spectra were taken on a Nicolet iS50 (Thermo Fisher Scientific) spectrometer with a DTGS detector. For the collection of temperature-variable FTIR spectra, the PIE₉ sample with suitable thickness was prepared and coated on a ZnSe tablet during heating from 30–100 °C with an interval of 1 °C. 2D correlation spectroscopy (2Dcos) analysis was performed on the software 2D Shige ver. 1.3 (Shigeaki Morita, Kwansei-Gakuin University, Japan, 2004–2005) with temperature-resolved FTIR spectra and further plotted into contour maps by Origin, ver. 9.8. In the 2Dcos maps, warm colors (red) represent positive intensities, while cold colors (blue) represent negative ones. XPS were collected with Thermo Scientific K-Alpha. The solid-state NMR spectra was recorded on Bruker Avance Neo 400WB.

The tests of the ionic skin on human skin and fingers (approved by the Institutional Biomedical Research Ethics Committee of Shanghai Institutes for Biological Sciences (NO. 3011-19-03)) do not affect living people physically or physiologically, and the authors did not seek or receive identifiable private information.

Supporting Information

Supporting Information is available from the Wiley Online Library or from the author.

Acknowledgements

The authors gratefully acknowledge the financial support of the National Natural Science Foundation of China (NSFC) (Nos. 52161135102, 51973035, 21803010) and the Research Foundation of National Innovation Center of Advanced Dyeing & Finishing Technology (No. 2022GCJJ07).

Conflict of Interest

The authors declare no conflict of interest.

Data Availability Statement

The data that support the findings of this study are available from the corresponding author upon reasonable request.

Keywords

hydrogen bonds, liquid-free, lithium bonds, mechanical robustness, photonic ionic elastomers

Received: December 5, 2022

Revised: February 28, 2023

Published online: March 31, 2023

- [1] a) J. Wang, B. Wu, P. Wei, S. Sun, P. Wu, *Nat. Commun.* **2022**, *13*, 4411; b) Y. Liu, K. He, G. Chen, W. R. Leow, X. Chen, *Chem. Rev.* **2017**, *117*, 12893; c) T. R. Ray, J. Choi, A. J. Bandodkar, S. Krishnan, P. Gutruf, L. Tian, R. Ghaffari, J. A. Rogers, *Chem. Rev.* **2019**, *119*, 5461; d) C. Kaspar, B. J. Ravoo, W. G. van der Wiel, S. V. Wegner, W. H. P. Pernice, *Nature* **2021**, *594*, 345.
- [2] a) W. Zhang, B. Wu, S. Sun, P. Wu, *Nat. Commun.* **2021**, *12*, 4082; b) Y. Wang, S. Sun, P. Wu, *Adv. Funct. Mater.* **2021**, *31*, 2101494; c) M. Wang, Y. Luo, T. Wang, C. Wan, L. Pan, S. Pan, K. He, A. Neo, X. Chen, *Adv. Mater.* **2021**, *33*, 2003014.
- [3] a) Z. Zhang, Z. Chen, Y. Wang, Y. Zhao, *Proc. Natl. Acad. Sci. USA* **2020**, *117*, 18310; b) Y. Wang, L. Shang, G. Chen, L. Sun, X. Zhang, Y. Zhao, *Sci. Adv.* **2020**, *6*, aax8258.
- [4] J. Teyssier, S. V. Saenko, D. van der Marel, M. C. Milinkovitch, *Nat. Commun.* **2015**, *6*, 6368.
- [5] a) Y. He, L. Liu, Q. Fu, J. Ge, *Adv. Funct. Mater.* **2022**, *32*, 2200330; b) F. Meng, B. Ju, Z. Wang, R. Han, Y. Zhang, S. Zhang, P. Wu, B. Tang, *J. Am. Chem. Soc.* **2022**, *144*, 7610; c) D. Yang, S. Ye, J. Ge, *J. Am. Chem. Soc.* **2013**, *135*, 18370.
- [6] a) M. Li, H. Tan, L. Jia, R. Zhong, B. Peng, J. Zhou, J. Xu, B. Xiong, L. Zhang, J. Zhu, *Adv. Funct. Mater.* **2020**, *30*, 2000008; b) H. Tan, Q. Lyu, Z. Xie, M. Li, K. Wang, K. Wang, B. Xiong, L. Zhang, J. Zhu, *Adv. Mater.* **2019**, *31*, 1805496.
- [7] a) C. Larson, B. Peele, S. Li, S. Robinson, M. Totaro, L. Beccai, B. Maz-zolai, R. Shepherd, *Science* **2016**, *351*, 1071; b) X. Shi, Y. Zuo, P. Zhai, J. Shen, Y. Yang, Z. Gao, M. Liao, J. Wu, J. Wang, X. Xu, Q. Tong, B. Zhang, B. Wang, X. Sun, L. Zhang, Q. Pei, D. Jin, P. Chen, H. Peng, *Nature* **2021**, *591*, 240.
- [8] Q. Lyu, M. Li, L. Zhang, J. Zhu, *Macromol. Rapid. Commun.* **2022**, *43*, 2100867.
- [9] a) Y. Wang, X. Cao, J. Cheng, B. Yao, Y. Zhao, S. Wu, B. Ju, S. Zhang, X. He, W. Niu, *ACS Nano* **2021**, *15*, 3509; b) L. Bai, Y. Jin, X. Shang, H. Jin, Y. Zhou, L. Shi, *J. Mater. Chem. A* **2021**, *9*, 23916.
- [10] a) Q. Lyu, S. Wang, B. Peng, X. Chen, S. Du, M. Li, L. Zhang, J. Zhu, *Small* **2021**, *17*, 2103271; b) Y. Sun, Y. Wang, Y. Liu, S. Wu, S. Zhang, W. Niu, *Adv. Funct. Mater.* **2022**, *32*, 2204467.
- [11] L. Shi, T. Zhu, G. Gao, X. Zhang, W. Wei, W. Liu, S. Ding, *Nat. Commun.* **2018**, *9*, 2630.
- [12] a) X. Ming, C. Zhang, J. Cai, H. Zhu, Q. Zhang, S. Zhu, *ACS Appl. Mater. Interfaces* **2021**, *13*, 31102; b) J. Wei, Y. Zheng, T. Chen, *Mater. Horiz.* **2021**, *8*, 2761.
- [13] R. Matsuoka, M. Shibata, K. Matsuo, R. Sai, H. Tsutsumi, K. Fujii, Y. Katayama, *Macromolecules* **2020**, *53*, 9480.
- [14] G. H. Lee, T. M. Choi, B. Kim, S. H. Han, J. M. Lee, S. H. Kim, *ACS Nano* **2017**, *11*, 11350.
- [15] X. Qu, W. Niu, R. Wang, Z. Li, Y. Guo, X. Liu, J. Sun, *Mater. Horiz.* **2020**, *7*, 2994.
- [16] G. H. Lee, S. H. Han, J. B. Kim, J. H. Kim, J. M. Lee, S.-H. Kim, *Chem. Mater.* **2019**, *31*, 8154.
- [17] F. Asai, T. Seki, A. Sugawara-Narutaki, K. Sato, J. Odent, O. Coulembier, J. M. Raquez, Y. Takeoka, *ACS Appl. Mater. Interfaces* **2020**, *12*, 46621.
- [18] a) B. Yiming, Y. Han, Z. Han, X. Zhang, Y. Li, W. Lian, M. Zhang, J. Yin, T. Sun, Z. Wu, T. Li, J. Fu, Z. Jia, S. Qu, *Adv. Mater.* **2021**, *33*, 2006111; b) B. Yiming, Z. Zhang, Y. Lu, X. Liu, C. Creton, S. Zhu, Z. Jia, S. Qu, *Macromolecules* **2022**, *55*, 4665.
- [19] a) E. Miwa, K. Watanabe, F. Asai, T. Seki, K. Urayama, J. Odent, J.-M. Raquez, Y. Takeoka, *ACS Appl. Polym. Mater.* **2020**, *2*, 4078; b) K. Watanabe, E. Miwa, F. Asai, T. Seki, K. Urayama, T. Nakatani, S. Fujinami, T. Hoshino, M. Takata, C. Liu, K. Mayumi, K. Ito, Y. Takeoka, *ACS Mater. Lett.* **2020**, *2*, 325.
- [20] S. W. Cranford, A. Tarakanova, N. M. Pugno, M. J. Buehler, *Nature* **2012**, *482*, 72.
- [21] a) W. Ren, P. J. McMullan, A. C. Griffin, *Phys. Status Solidi B* **2009**, *246*, 2124; b) M. O. Saed, W. Elmadih, A. Terentjev, D. Chronopoulos, D. Williamson, E. M. Terentjev, *Nat. Commun.* **2021**, *12*, 6676.
- [22] a) L. Bai, Y. Jin, X. Shang, L. Shi, H. Jin, R. Zhou, S. Lai, *Chem. Eng. J.* **2022**, *438*, 135596; b) Y. Wang, Y. Yu, J. Guo, Z. Zhang, X. Zhang, Y. Zhao, *Adv. Funct. Mater.* **2020**, *30*, 2000151; c) H. Zhang, J. Guo, Y. Wang, L. Sun, Y. Zhao, *Adv. Sci.* **2021**, *8*, 2102156; d) H. Zhang, H. Chen, J. H. Lee, E. Kim, K. Y. Chan, H. Venkatesan, M. H. Adegun, O. G. Agbabiaka, X. Shen, Q. Zheng, J. Yang, J. K. Kim, *Adv. Funct. Mater.* **2022**, *32*, 2208362; e) X. Li, J. Liu, Q. Guo, X. Zhang, M. Tian, *Small* **2022**, *18*, e2201012.
- [23] Y.-J. Wang, J. Li, Z. Xu, B. Liu, Y. Zhao, L. Chen, W. Liu, *Chem. Eng. J.* **2021**, *417*, 127967.
- [24] Y. Liu, L. Hou, Y. Jiao, P. Wu, *ACS Appl. Mater. Interfaces* **2021**, *13*, 13319.
- [25] Z. Jin, T. Chen, Y. Liu, W. Feng, L. Chen, C. Wang, *J. Am. Chem. Soc.* **2023**, *145*, 3526.
- [26] X. Chen, Y. K. Bai, C. Z. Zhao, X. Shen, Q. Zhang, *Angew. Chem., Int. Ed.* **2020**, *59*, 11192.
- [27] a) D. M. Seo, S. Reininger, M. Kutcher, K. Redmond, W. B. Euler, B. L. Lucht, *J. Phys. Chem. C* **2015**, *119*, 14038; b) N. Chapman, O. Borodin, T. Yoon, C. C. Nguyen, B. L. Lucht, *J. Phys. Chem. C* **2017**, *121*, 2135.
- [28] a) I. Noda, *J. Am. Chem. Soc.* **1989**, *111*, 8116; b) K. Gong, L. Hou, P. Wu, *Adv. Mater.* **2022**, *34*, 2201065; c) Q. Gong, L. Hou, T. Li, Y. Jiao, P. Wu, *ACS Nano* **2022**, *16*, 8449.
- [29] M. J. Lee, J. Han, K. Lee, Y. J. Lee, B. G. Kim, K. N. Jung, B. J. Kim, S. W. Lee, *Nature* **2022**, *601*, 217.
- [30] W. Niu, X. Cao, Y. Wang, B. Yao, Y. Zhao, J. Cheng, S. Wu, S. Zhang, X. He, *Adv. Funct. Mater.* **2021**, *31*, 2009017.
- [31] M. Li, B. Zhou, Q. Lyu, L. Jia, H. Tan, Z. Xie, B. Xiong, Z. Xue, L. Zhang, J. Zhu, *Mater. Chem. Front.* **2019**, *3*, 2707.
- [32] J. H. Kim, G. H. Lee, J. B. Kim, S. H. Kim, *Adv. Funct. Mater.* **2020**, *30*, 2001318.
- [33] Y. Hao, D. Feng, L. Hou, T. Li, Y. Jiao, P. Wu, *Adv. Sci.* **2022**, *9*, 2104832.